


PSFC/JA-01-7

**Electron Cyclotron Emission Refraction Effects
During Edge Localized Modes**

View metadata, citation and similar papers at core.ac.uk

brought to you by  **CO**
provided by DSpace@

Y. In, A.E. Hubbard, I.H. Hutchinson

April 2001

Plasma Science and Fusion Center
Massachusetts Institute of Technology
Cambridge, MA 02139 USA

This work was supported by the U.S. Department of Energy, Cooperative Grant No. DE-FC02-99ER54512. Reproduction, translation, publication, use and disposal, in whole or in part, by or for the United States government is permitted.

Submitted for publication to Plasma Physics and Controlled Fusion.

Electron Cyclotron Emission Refraction Effects during Edge Localized Modes

Y In, A E Hubbard, I H Hutchinson

MIT Plasma Science and Fusion Center, Cambridge, MA 02139

E-mail: yongkin@psfc.mit.edu

Abstract. During ‘Type III’ ELMs on Alcator C-Mod, electron cyclotron emission (ECE) diagnostics show brief signal drops of second harmonic X-mode and signal increases of fundamental harmonic O-mode. These are explained in terms of refraction effects and found to be useful to infer the associated ELM geometrical dimensions. A new ray tracing code, which can accommodate poloidal variations, has been developed for this investigation. The ELMs are modeled satisfactorily as a density loss from a poloidally elongated region.

PACS numbers: 42.15.-i,52.25.Sw,52.55.Fa,52.70.Gw

1. Introduction

Edge localized modes (ELMs) are ‘MHD activity with quasi-periodic bursts localized at plasma edges’ [1]. During the MHD events, particles are expelled from the main plasma and the energy confinement degrades, typically by $\sim 15\%$ [2]. ELMs, however, provide not only detrimental but also beneficial effects. For example, while ELM-free H-mode can be degraded by accumulated impurities, we can take advantage of ELMs to regulate impurities without suffering H to L back transitions. Nevertheless, some big ELMs (so called Type I or ‘Giant’ ELMs) seem to be more troublesome because they can damage the first wall surface materials, in that the associated heat loads to the wall exceed the limits the surface materials can endure. Thus, the understanding of ELMs has been one of the key tokamak physics issues for more than a decade. Although they are not perfectly understood yet, there is a widespread opinion that some ELMs (e.g. Type I ELMs) can be explained in terms of ideal MHD instability. There is less theoretical consensus regarding smaller ELMs, such as Type III ELMs [3].

In terms of experimental observations, ELMs challenge the spatiotemporal resolution of most diagnostics because they are not only localized at the plasma edge but also change rapidly in time. This is a primary reason that ELM geometric structure has not been measured. Before and after some ELMs, important parameters such as pedestal width and height and pressure gradient have been studied in various machines (JT-60U, JET, DIII-D, ASDEX-UG, Alcator C-Mod) [4, 5, 6, 7, 8]. Meanwhile, during an ELM event itself, ASDEX-UG was the first tokamak capable of measuring the electron

temperature and density profiles [9]. Nevertheless, only Type I ELMs, which have bigger perturbations than any other type of ELMs, have been measured in ASDEX-UG, while Type III ELMs have not. Even for the measured Type I ELMs, the poloidal structure has not been resolved. In this paper, however, a new method is presented which has the potential to infer ELM geometrical dimensions indirectly via ECE diagnostics [10], which may provide not only radial but also poloidal structures of ELMs. This is based on ECE refraction effects in high density plasmas, which are significant in the vicinity of the high (poloidal) density gradient. This approach does not determine a complete 2-D structure unequivocally without additional information yet.

In Sec. 2, experimental observations of the ELMs in C-Mod [11] are presented. In Sec. 3, the signal dips seen on the ECE diagnostic during Type III ELMy bursts are analyzed in terms of refraction effects. Specifically, in Sec. 3. 3.1, a newly developed ray tracing code is discussed and compared with a conventional code, TORAY [12]. In Sec. 3. 3.2, the ray trajectories are calculated and the ECE signal changes for various density perturbation models are evaluated. In Sec. 4, the uncertainties of the ELM dimensions inferred from experimental observations are discussed. In addition, the signal evolution is interpreted in terms of poloidal rotation. Results are summarized in Sec. 5.

2. Experimental observation

2.1. Diagnostics

Alcator C-Mod is a high field ($B_T = 5 - 8$ T), compact ($R = 0.67$ m major radius, $a = 0.22$ m minor radius), diverted tokamak. Poloidal magnetic field pickup loops measure fluctuations with a digitization rate of 1 or 2 MHz. For fluctuation studies, there were four sets of toroidally displaced coils located on outboard limiters. For electron temperature measurements, a grating polychromator (GPC) and a heterodyne radiometer are primarily used for this analysis. The GPC measures the extraordinary mode (X-mode) of emission at the second harmonic ($2\Omega_{ce}$) of the electron cyclotron frequency, while the radiometer (110 - 128 GHz) detects the fundamental harmonic (Ω_{ce}) ordinary mode (O-mode) ECE. The GPC has 9 channels and provides relatively good spatial resolution (~ 1 cm) and temporal response (to $2 \mu\text{sec}$). The fundamental O-mode radiometer has better spatial resolution (0.2 - 0.5 cm) with similar temporal resolution. However, the usage of the O-mode radiometer for T_e measurements is limited to low density plasmas because the O-mode density cutoff condition is exceeded during most H-modes. Using Thomson scattering, the electron temperature and density profiles are obtained sparsely in time and space[13].

Since the time of the ELM measurements reported here, various high resolution edge diagnostics, such as edge Thomson Scattering, bremsstrahlung and soft X-ray profile measurement, have been added for pedestal studies[14]. Although these are not able to resolve the time evolution during small ELMs, they should provide additional

information on equilibrium profiles for future measurements.

2.2. Observation of edge localized modes (ELMs)

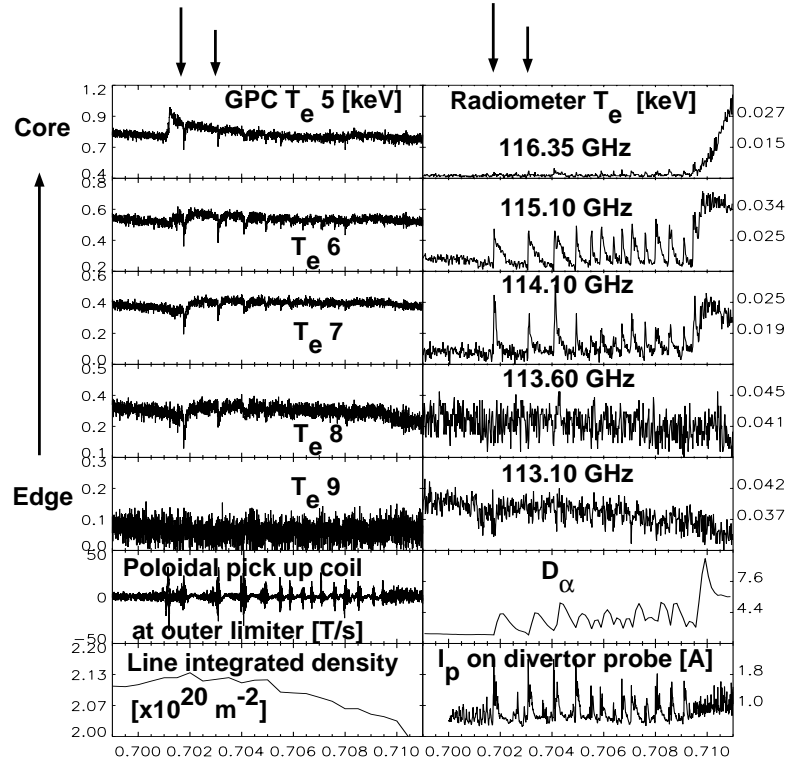


Figure 1. Signal drops on the 2nd harmonic X-mode GPC at each ELM (marked by arrow), while signal increases on the fundamental harmonic O-mode radiometer. On the ion saturation current of divertor probe, similar spikes are observed. The magnetics show the toroidal mode number (n) is as high as 14.

Fig. 1 shows the experimental observation of rather unusual Type III ELMy bursts. On the left top five time traces, we can clearly see that there are signal drops during Type III ELMs on GPC. At first, it was surprising to see T_e drops on core channels because ELMs are generally considered to be “edge-localized”. On the other hand, positive signal spikes are seen on the right five time traces, which show signals from the

fundamental harmonic O-mode radiometer. At the same time, on a divertor Langmuir probe, similar spikes were observed in ion saturation currents, which implies that there were intermittent radial particle fluxes coming from the main plasma. Based on the magnetic analysis, the associated toroidal mode number of this particular case was ~ 14 . Negligible signals were observed on inboard magnetic pick up loops, providing evidence that this type of MHD has ‘ballooning’ character. It should be noted that such signal drops on GPC were observed only in rather high density plasmas ($\bar{n}_e > 3.0 \times 10^{20} m^{-3}$).

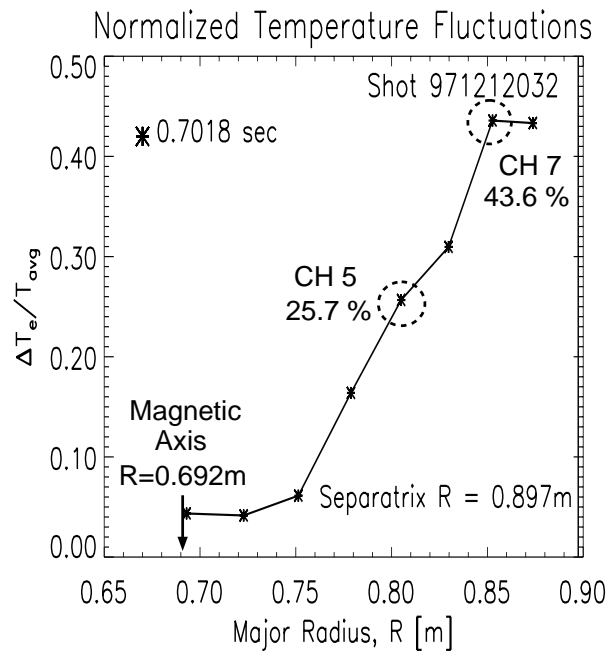


Figure 2. Fractional changes of GPC during Type III ELM bursts. Overall, 10 - 50 % fractional changes were observed. In particular, the changes (26 and 44 %) of Ch 5 and Ch 7 are used in the following analysis to check whether a model is appropriate or not.

Fig. 2 shows the fractional changes of the GPC during the Type III ELMy bursts. The electron temperature fractional changes are defined as $\Delta T_e/T_{avg} \equiv (T_{max} - T_{min})/T_{avg}$. Ch 5 and Ch 7 showed approximately 25.7 and 43.6 % drops.

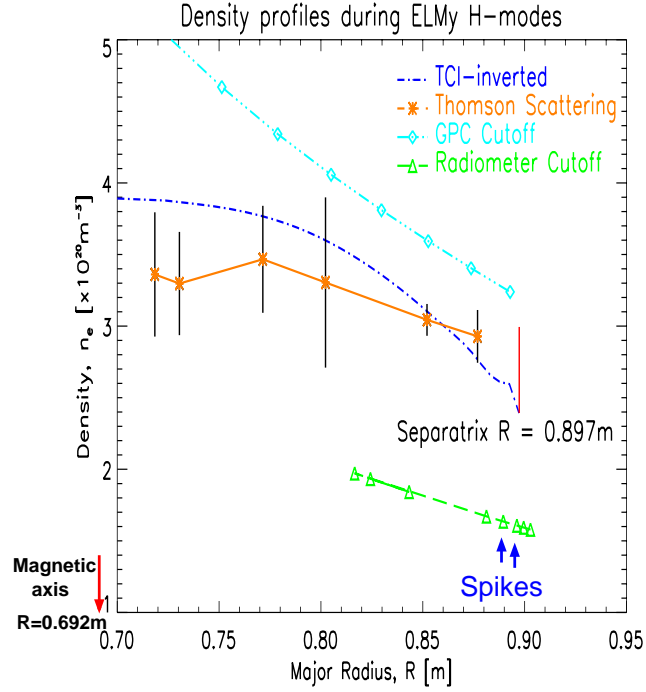


Figure 3. Density profiles based on measurements and cutoff conditions. TCI-inverted and Thomson scattering density profiles are from measurements. The GPC and radiometer cutoff density profiles are derived from the density cutoff conditions associated with the second harmonic of X-mode and the fundamental harmonic of O-mode respectively.

Fig. 3 shows all the associated density profiles at the approximate time of the ELMy bursts. The GPC and radiometer cutoff densities vs R are based on the conditions of $\omega_{pe}^2/\Omega_{ce}^2 = 2$ and $\Omega_{ce} = \omega_{pe}$ respectively, where Ω_{ce} is the electron cyclotron frequency and ω_{pe} plasma frequency. One explanation for the signal drops is that there could be

density increase at the ELM so as to cut off the central channels. However, this would be inconsistent with the observation that the signals on some edge channels of the O-mode radiometer increased. On the other hand, the refraction effect is a good candidate to explain such signal drops in that any ray trajectory is affected by the first derivative of the refractive index, not only by the value of refractive index itself.

3. Refraction effects during ELMs

3.1. Ray tracing code

In the past, a ray tracing code in the electron cyclotron frequency range called TORAY has been successful for general purposes. However, it does not accommodate any poloidal variations. For the ELM models considered here, poloidal variation is essential for modeling refraction effects. Hence, a new ray tracing code that is capable of handling poloidal changes was needed and has been developed.

3.1.1. Ray equations For perpendicular propagation of X-mode waves, the dispersion determinant $D = D[N, \Omega_{ce}^2, \omega_{pe}^2, \omega]$ becomes

$$D = 1 - N^2 - \left(\frac{\omega_{pe}}{\omega}\right)^2 \frac{\omega^2 - \omega_{pe}^2}{\omega^2 - \omega_{UH}^2} \quad (1)$$

where $N^2 = (ck/\omega)^2$, $\omega_{pe}^2 \propto n(\mathbf{x})$ (density) and $\Omega_{ce} \propto |\mathbf{B}(\mathbf{x})|$ (magnetic field). The ray equations can be found as follows [12];

$$\frac{d\mathbf{x}}{dt} = -\frac{\partial D}{\partial \mathbf{k}}, \quad \frac{d\mathbf{k}}{dt} = \frac{\partial D}{\partial \mathbf{x}}, \quad (2)$$

$$\frac{d\mathbf{x}}{ds} = -\operatorname{sgn}\left(\frac{\partial D}{\partial \omega}\right) \frac{\frac{\partial D}{\partial \mathbf{k}}}{\left|\frac{\partial D}{\partial \mathbf{k}}\right|}, \quad \frac{d\mathbf{k}}{ds} = \frac{\frac{\partial D}{\partial \mathbf{x}}}{|\mathbf{V}_g| \frac{\partial D}{\partial \omega}},$$

where \mathbf{V}_g ($\equiv \frac{d\mathbf{x}}{dt}$) is group velocity and $s = |\mathbf{V}_g|t = \left|\frac{d\mathbf{x}}{dt}\right|t$ is the arc-length. Considering the axisymmetric characteristics of the tokamak, no toroidal angle dependency is included for this analysis. The position vector (\mathbf{x}) and its wavevector (\mathbf{k}) can then be described in 2-dimensional form; i.e. $\mathbf{x} = \mathbf{x}(x, y)$, $\mathbf{k} = \mathbf{k}(k_x, k_y)$. Thus, the solutions of the four coupled ordinary differential equations provide the ray trajectory.

3.1.2. Benchmarking with TORAY code To benchmark the newly developed code with TORAY, a simple parabolic, poloidally symmetric, density profile was assumed and some sample ray trajectories were found for low ($n_0 = 4 \times 10^{20} m^{-3}$) and high ($n_0 = 7 \times 10^{20} m^{-3}$) density cases. As shown in Fig. 4, the ray trajectories agreed well. The slight difference between TORAY and the new code near the resonant layer in Fig. 4 a) comes from the fact that thermal effects are considered in TORAY, while the new code is based only on the cold plasma approximation. However, since we are interested in the location of the beam at the resonance layer, rather than the absorbed power, such thermal effects are not significant for the ELM analysis considered here. The case in which the density exceeds the wave cutoff has also been ascertained to give proper reflection in both calculations, as shown in Fig. 4 b).

3.2. Refracted ray trajectories

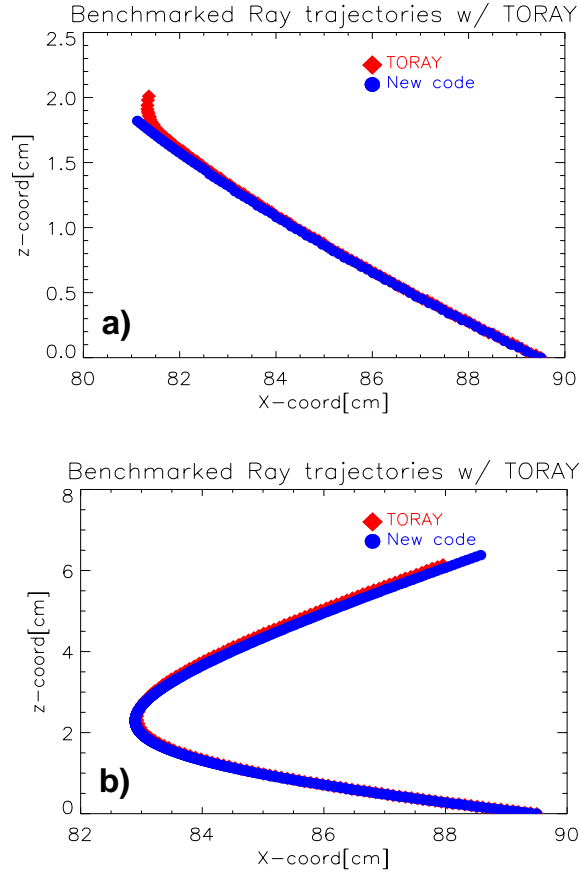


Figure 4. Benchmarks with TORAY using a new ray tracing code. Both the ray trajectories agree well. (a) The resonance layer is located at $R=81.3$ cm for low density case. (b) Near $R=82.9$ cm, cutoff occurred and the ray trajectories reflected back for high density case.

3.2.1. Density models including poloidal variations Four types of density models have been considered; a) reference b) hump c) dip d) dip without bank cases. All the other density profiles are compared with a reference density profile (monotonic). The reference density profile ($n_0 = 3.66 \times 10^{20} m^{-3}$) has been determined from the Thomson Scattering (See Fig. 3).

The four types of density profiles at the midplane are shown in Fig. 5. The density hump case [Fig. 5 b)] explains the signal drops on GPC with the smallest density

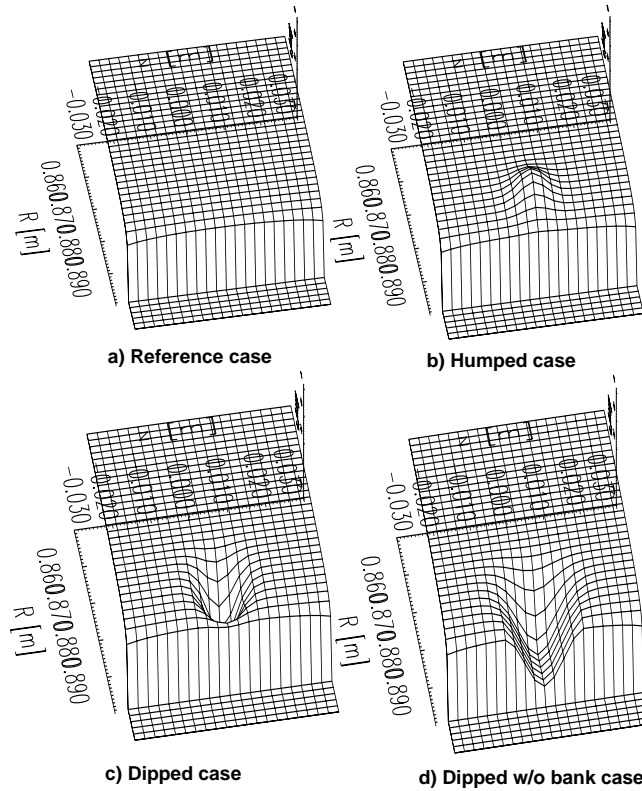


Figure 5. Density models near the midplane. The reference case a) has a typical monotonic density profile. Models b), c) and d) have been constructed to describe the ELMy phenomena. The model d) turns out to be the most likely.

perturbation. However, it does not explain the signal spikes observed on fundamental O-mode radiometer. In particular, considering that spikes occurred in a period when O-mode emission was normally cut off, the local density near the channels showing spikes must be lower than between ELMs. The opposite case [density dip case, Fig. 5 c)] has also been investigated. However, this model has a ‘bank’ next to the density trough, that would prevent the fundamental harmonic O-mode radiometer from receiving emission. The most plausible density profile is therefore considered to be a density dip without edge bank, as shown in Fig. 5 d). In this model, particles are ejected from the main

plasma and the edge density decreases monotonically in R .

The analytical form adopted for this analysis is as follows;

$$n[x, y] = n_0 \left[1 - \frac{x^2 + \frac{y^2}{\kappa^2}}{a^2} \right]^\alpha \pm \sum_{j=1}^N q_j n_0 \exp \left[- \left(\frac{s_j}{b_j} \right)^2 \right] \quad (3)$$

where n_0 is peaked density, a minor radius, κ elongation, α peakedness, N number of humps (dips), j j -th hump (dip),

$$s_j \equiv \sqrt{\{(x - \alpha_j) \cos \theta_j + (y - \beta_j) \sin \theta_j\}^2 + \frac{\{(x - \alpha_j) \sin \theta_j + (y - \beta_j) \cos \theta_j\}^2}{\kappa_j^2}}$$

s_j pseudo distance, q_j weighting, b_j half of the hump (dip) width, θ_j tilted angle, κ_j hump (dip) elongation, and (α_j, β_j) hump (dip) center position.

When the second term of RHS of Eq. 3 is absent, it gives the reference case [Fig. 5 a)].

When the sign of this term is positive or negative, it represents the humped and dipped cases respectively. For the model d), the density is the same as the model c) up to the radial position of the density trough, while the density and poloidal density gradients outside of the density trough have been set to be equal to those at the density trough.

There are many free parameters in these models, including the width (b_j), height (q_j), elongation (κ_j), rotation angle (θ_j), and radial position (α_j, β_j), as schematically shown in Fig. 6. The subscript j of each parameter in this figure is omitted for convenience. The density perturbation is assumed to be poloidally displaced by θ_j , which is measured from the ECE collection optics located at the midplane. The radial position of the density perturbation has been fixed near $R=0.89$ m, which is 1 cm away from the last closed flux surface (LCFS). This was determined from the O-mode radiometer observation, in which the signal spikes were located near $R=0.89$ m, while

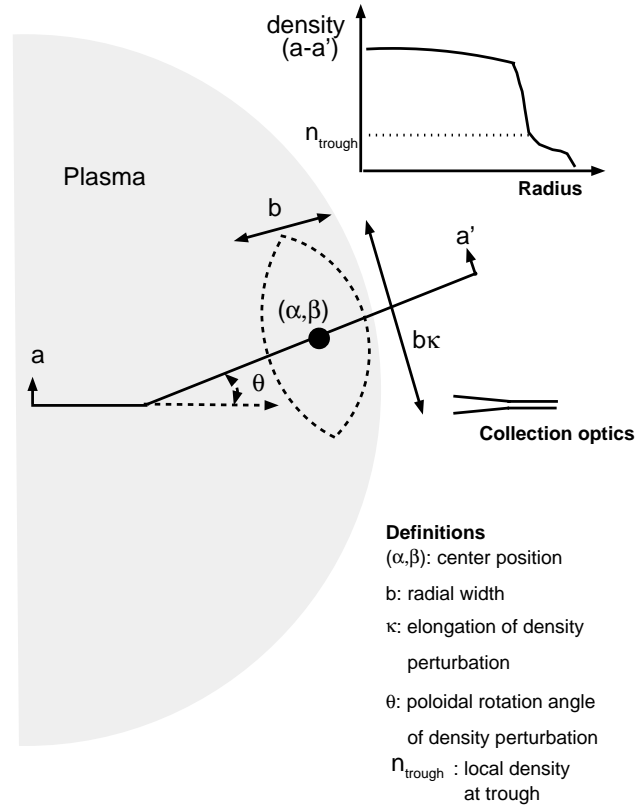


Figure 6. Schematics of key parameters. The schematic density profile (a-a') shows the local density height (i.e. n_{trough}). All the parameters are defined in the text.

no other channels of the O-mode radiometer showed changes. In addition, the local density of the center of ELMs at the midplane should be less than the cutoff density of the associated channels ($\approx 1.5 \times 10^{20} \text{m}^{-3}$) of the O-mode radiometer. A value of $0.5 \times 10^{20} \text{m}^{-3}$ was used for most runs. The rotation angle ($\theta=0$) has been set to have the center of ELMs located at the midplane, since a density perturbation located at the midplane proves to give the most signal change. Hence, we may take advantage of the up-down symmetry of the ray trajectories. The variation of the signal changes with θ is shown in Sec 4. 4.2. The width and elongation characterize the physical dimensions of

the radial and poloidal density perturbation at each ELM and have been varied in the ray tracing code. Typical refractive index profiles at the midplane for each of the four models and for two wave frequencies are shown in Fig. 7. Since the frequency of Ch 5 (256.4 GHz) is higher than that of Ch 7 (241.3 GHz), its $N(R)$ changes more slowly.

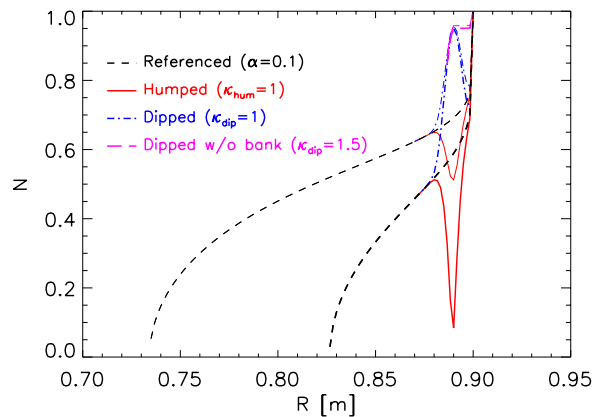


Figure 7. Refractive index profiles at the midplane. $n_0=3.66\times 10^{20}m^{-3}$ and $n_{trough}^{ELM}=0.5\times 10^{20}m^{-3}$.

3.2.2. Ray trajectories in vacuum collection optics The collection optics outside of the main plasma define which rays leaving the plasma will be detected. To provide starting rays, the optical system has been modeled. Two elliptical focusing mirrors with a minor diameter of 20.3 cm, a major diameter of 28.7 cm and $f = 2.7$ m focal length form a gaussian telescope, with a total length of $4f=10.8$ m between the plasma image and the defining aperture [16]. The aperture of the collection optics is a 3 cm \times 5 cm rectangle, with the poloidal length narrower. The detector aperture was modeled as a 3 cm diameter circle. Based on this model, the one-to-one corresponding rays between object and image on the detector have been found using OPTICA [17] and used for

reference values for further ray tracing analysis.

3.2.3. Ray trajectories in the main plasma The main purpose of this investigation is to see whether the rays which are accepted by the collection optics are refracted by ELMs so that they see colder regions. To minimize the number of calculations, a reciprocal method has been used, in which ray tracing is performed from vacuum into plasma, rather than from plasma to vacuum. Best fit parameters have been found for each model, as described below.

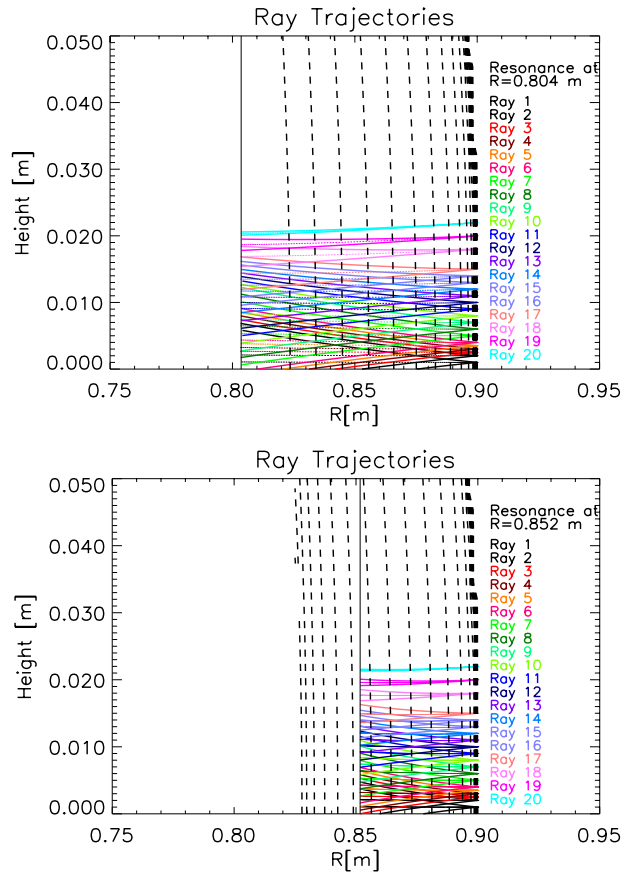


Figure 8. Ray trajectories of Channel 5 and 7, whose resonance layers are at $R = 0.804$ m and 0.852 m respectively. For the reference profile, note all the rays are near the midplane.

Each density perturbation model has been fully explored in terms of its width and elongation. As shown in Fig. 8, three ray trajectories leaving from each point at a specific height were investigated; upper, middle and lower angle cases. The upper and lower angles were determined from the vacuum collection optics, while the middle angle is the arithmetic average of the two limiting angles. In general, the variations between the upper and lower angle rays were not significant in terms of height and temperature (z, T_e). Thus, to interpret the results in terms of their effect on temperature measurements, only the middle rays have been used. To minimize any calculation errors, the mesh size (Δz) between two adjacent points was chosen to be no more than 3.8 mm. Fig. 8 shows the reference case with no perturbation, where all the rays of Ch 5 and Ch 7 are concentrated within 2 cm of the midplane, as they should be. The dashed lines show contours of refractive index, with spacing 0.025 for Ch 5 and 0.05 for Ch 7, and the solid vertical lines the cyclotron resonant layers for each frequency.

Fig. 9 shows the case with constant n_e outside a density dip [model d)]. 60 vertical positions were used for this calculation but only the middle ray is used. It was checked for a few cases that taking 180 rays does not change the pattern. The contour plot of the ELM shows the refractive index is varying only in the poloidal direction outside a certain radial position near the LCFS. There is a certain poloidal position slightly off the midplane where the ray trajectories are refracted most. The radial and poloidal lengths of the perturbed region were found to be critical to the ray trajectories. Details of refraction calculating for other parameters and density models can be found in Ref.

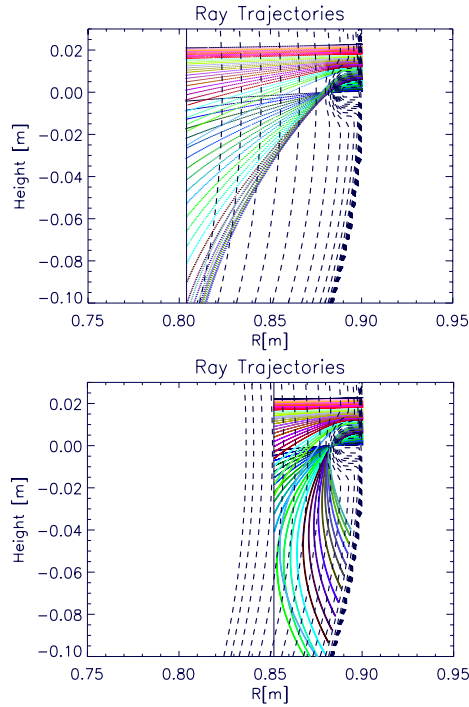


Figure 9. Ray trajectories of Channel 5 and 7 for model d). Due to the density dip without a bank at larger radii, the ray trajectories are bent enough to be consistent with the experimental observation. 23.2 and 41.8 % signal changes respectively are estimated using Gaussian weighting, while 21.3 and 39.1 % signal changes are estimated using constant weighting.

[15].

3.2.4. Estimation of ECE signal perturbation All the physical quantities, including electron temperature (T_e) and density (n_e), are assumed to be constant at each flux surface, except in the vicinity of the perturbation. Rays are traced until they either encounter the electron cyclotron layer or leave the modeling region. The intensity for each ray is given by the radiation temperature where it encounters the layer (or zero if

it leaves the plasma). The total collected signal (I) is approximated by

$$I = \sum_j I_j = (const) \cdot \sum_j T_j(A\Omega)_j w_j \quad (4)$$

where T_j is the temperature from blackbody radiation at the emission layer (assuming ‘optically thick’ plasmas), $A\Omega$ is the etendue with area A and solid angle Ω , and w_j is the weighting. The signal changes can then be found by

$$\frac{\Delta I}{I} = \frac{I - I'}{I} = \frac{\sum_j [T_j - T'_j](A\Omega)_j w_j}{\sum_j T_j(A\Omega)_j w_j} \quad (5)$$

where I and I' are the signal intensities before and during the ELM perturbation respectively. The weighting factors (w_j) associated with the aperture cannot be described as a simple step function and need to be determined considering the edge effects, or, so called ‘vignetting’. According to Hsu’s investigation of the aperture edge effects in our optical system [16], the actual weighting is given by the dashed curve in Fig. 10.

Two extreme weightings (Gaussian and constant) drawn in solid curves of Fig. 10 were considered in the calculations, which turn out to be only weakly dependent on the shape of weighting factors.

Table 1. Signal changes of each model

Perturbed density model		Gaussian		Constant	
		Ch 5	Ch 7	Ch 5	Ch 7
Hump	($\kappa_{hump}=1.0$)	7.4	49.5	4.5	26.6
Dip	($\kappa_{dip}=1.0$)	16.0	45.2	10.7	33.5
Dip without edge bank	($\kappa_{dip}=1.0$)	41.2	44.9	32.8	39.7
	($\kappa_{dip}=1.5$)	23.2	41.8	21.3	39.1
Experiment		Ch 5 - 25.7		Ch 7 - 43.6	

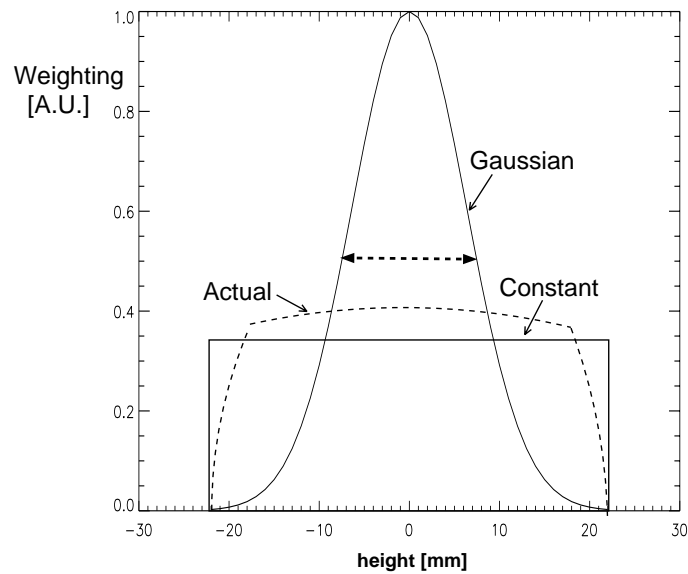


Figure 10. Weighting function ($w_j = w_j(z)$). In practice, the vignetting at the edge of the ECE collection optics aperture requires weighting factors, as shown in the dashed curve. Two extreme cases (Gaussian and constant weighting) were considered in these calculations. The signal change estimation is only weakly dependent on the shape of weighting factors.

Considering all the aforementioned contributions, Table 1 summarizes the signal changes of Ch 5 and Ch 7 for the three density models in comparison with experimental observation. Each case in this table was the best fit in that the estimated signal changes were closest to the experimentally observed changes. Depending on the type of weightings, there are some changes in hump and dip density models. However, for the dip without edge bank model, which is regarded as the most physically realistic, there are no significant changes between Gaussian and constant weightings. Thus, the

perturbed density model of a density dip without edge bank ($\kappa_{dip}=1.5$) is closest (within 5%) to the experimental observation. Although an ELM is edge-localized, it has been shown that it can affect even the core channels of ECE diagnostic due to refraction effects.

4. Interpretation of ELM perturbation

4.1. Uncertainties of the inferred dimensions

The ECE signal dips and spikes have been explained successfully in the previous section on the basis of a plausible density loss model [i.e. dip without edge bank model ($\kappa_{dip} = 1.5$)] using refraction effects. However, to infer various free parameters defined in Fig. 6, the uncertainties and limits need to be considered.

A ray's angular deviation ($\delta\theta$) due to a density perturbation can be represented approximately as

$$\delta\theta \propto (k_\theta \Delta r) \delta N, \quad (6)$$

where k_θ is a poloidal wave number, Δr radial width, and δN the refractive index change [18].

Since δN depends on δn_e , its uncertainty is dependent on the range of δn_e . The signal spikes observed on the fundamental O-mode radiometer suggest that the upper limit of the local density (n_{trough}^{ELM}) at R=0.89 m during an ELM is the corresponding cutoff density ($1.5 \times 10^{20} m^{-3}$). The lower limit is set by the fact that the density cannot be negative. Since the detailed edge density profiles near the time of ELM bursts were

not available, δN for Ch 5 and Ch 7 were uncertain, with possible ranges of 0.17 - 0.31 and 0.25 - 0.41 respectively. After extensive calculations, a value of $0.5 \times 10^{20} m^{-3}$ was found to be the best fit for n_{trough}^{ELM} . This value has been used for most subsequent runs.

Two parameters of k_θ and Δr are coupled together to describe the poloidally elongated density loss. Reducing one parameter and increasing the other by an equal amount cannot be distinguished in terms of the deviated angle ($\delta\theta$) calculated using refraction effects. Even if δN is known and fixed (based on $n_{trough}^{ELM} = 0.5 \times 10^{20} m^{-3}$), the refraction effect alone cannot determine the structures without relying on other information. However, if one parameter can be estimated, the other parameter can be easily determined using the refraction effects. For example, Δr can, in principle, be given from other edge diagnostics, such as the reflectometer. The k_θ could then be found using the refraction effects. Since no edge density profile was available during the rapidly varying ELM, a less reliable but reasonable estimate of Δr can be inferred from the O-mode radiometer. The inner channel at $R=0.88$ m, adjacent to the channels with signal spikes, suffered density cutoff continuously. Its cutoff density of $1.7 \times 10^{20} m^{-3}$ is therefore the lower limit of the local density at $R \sim 0.88$ m, which implies that Δr cannot be larger than 3 cm. Since the O-mode channels with signal spikes are located 1 cm inside from the LCFS, the lower limit of Δr is 1 cm.

Taking $\Delta r=2$ cm gave predicted signal drops closest to those observed for Ch 5 and 7 of GPC, while the other cases underestimated them. Within the limits of the models tried, $\Delta r=2$ cm was found to be the most likely. This is equivalent to the width (b), as

defined in Fig. 6. A poloidal $k_\theta=2.1 \text{ rad cm}^{-1}$ was then found to be reasonable using refraction effects, and is in a range consistent with magnetic analysis. The best way to minimize possible uncertainties may be from future direct measurements of Δr based on other edge diagnostics.

4.2. Signal time behavior

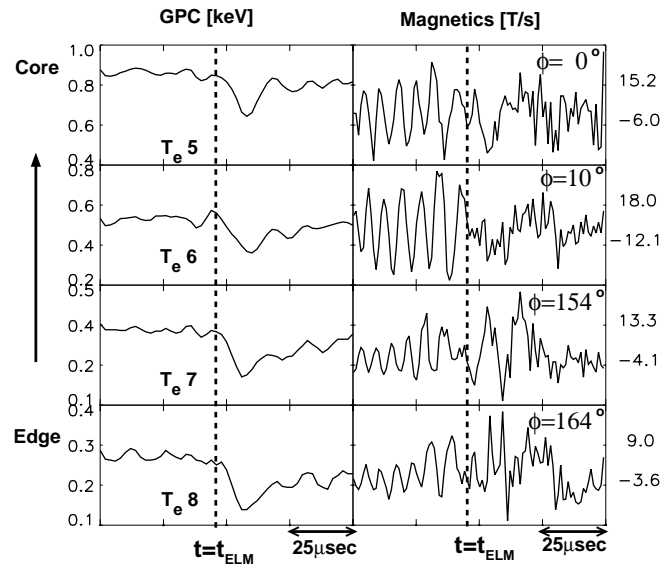


Figure 11. Time traces of GPC and magnetics near the ELM event. On GPC, there is no precursor, but during the ELM event, the signal drops almost linearly and recovers within $20 \mu\text{sec}$ in this case. On magnetics, the coherent precursors disappear in the midst of the ELM, which implies that ELMs probably become stochastic.

During the ELM event, the ECE signals are observed to decrease almost linearly for $\sim 10 \mu\text{sec}$, as shown in Fig. 11. The rate of change is well within the electronic bandwidth

of ~ 200 kHz. Two possible explanations for this are a poloidally rotating density perturbation and a density loss varying in time. To simulate the poloidal rotation, the center position of an ELM has been moved up and down.

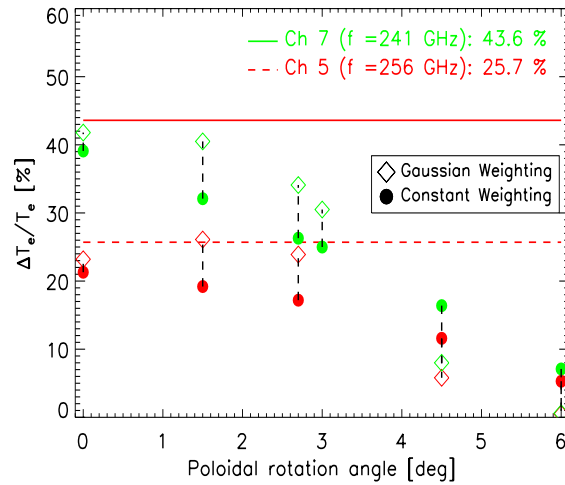


Figure 12. Fractional signal changes vs poloidal rotation angle of an ELM density perturbation model (dipped without edge bank case). As the poloidal rotation angle increases, the signal changes of both Ch 5 (dark tone) and Ch 7 (light tone) decrease nearly linearly. Here, the poloidal rotation angle θ is defined in Fig. 6. 6 degree is almost equivalent to 2.0 cm poloidal displacement of the ELM position. The dashed and solid horizontal lines represent the experimentally observed fractional changes of Ch 5 and Ch 7 of GPC respectively.

As shown in Fig. 12, as the ELM position moves poloidally away from the midplane, the fractional electron temperature changes drop almost linearly to zero for both low and high frequency channels. On the other hand, as shown in Fig. 13, if the density were

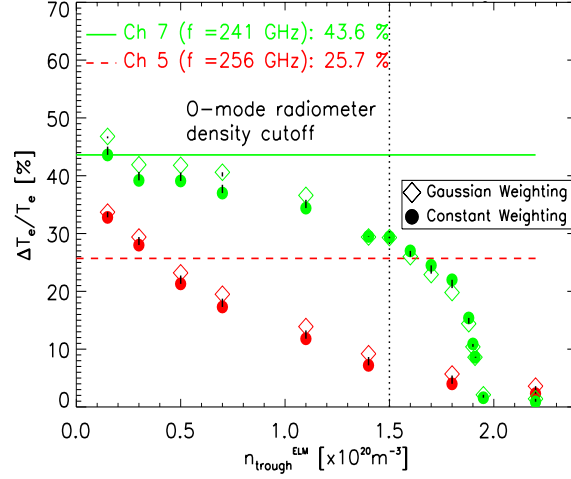


Figure 13. Fractional signal changes vs n_{trough}^{ELM} of a density perturbation model (dipped without edge bank case). As the minimum density of an ELM model increases, the fractional T_e changes of Ch 5 (dark tone) decrease almost linearly but those of Ch 7 (light tone) are not reduced much up to the O-mode radiometer cutoff density. On the other hand, as the n_{trough}^{ELM} increases further, the fractional changes of Ch 5 become negligible, while those of Ch 7 decrease nonlinearly down to insignificant levels.

to decrease steadily in time, below the level of the O-mode cutoff, the low frequency channel (Ch 7) is insensitive, while the signal of high frequency channel (Ch 5) would decrease linearly. This is inconsistent with the linear change seen experimentally on both channels. As a result, the poloidally rotating density perturbation model is found to be most appropriate to explain the linearly decreasing T_e signals on all channels.

5. Discussion and Conclusion

It has been observed that ELMs can affect even the core channels of an ECE diagnostic due to refraction effects, though they are edge-localized. The signal changes on the ECE diagnostic during ELMs are consistent with an ELM causing a poloidally and radially varying density loss. In particular, the radial and poloidal dimensions of n_e perturbation at Type III ELMs have been estimated on the basis of refraction effects on ECE diagnostics, combined with other available information.

Based on an edge density model, the ECE ray trajectories are found to be refracted enough to lead to reduced signals. A plausible ELM density profile was found by comparison with the experimental observations, which allowed the density perturbation and its geometry to be estimated. The following inferred dimensions on the basis of the plausible model are reasonable but not unique; radial width (Δr) ~ 1 to 3 cm, $\kappa_{dip} \sim 1.5$, $n_{trough}^{ELM} \sim 0.5 \times 10^{20} m^{-3}$ at the midplane 1cm inside from the LCFS. Using this model, the number of the particles expelled from the main plasma can be estimated. The upper limit of the estimated total particle loss related to each Type III ELM was 0.7 - 2 % even in the worst case. The typical repetition frequency of Type III ELMs is in the range of 1 - 3 kHz, but such repetitive ELMs are observed to occur for no more than tens of milliseconds. Furthermore, considering that ELMs are observed in other tokamaks to be localized not only radially and poloidally, but also toroidally, the actual particle loss due to ELMs is expected to be much smaller than the above estimate. Unfortunately, C-Mod does not have direct edge density measurements with sufficient

time resolution to resolve ELM perturbations directly. The outer channel of the far infrared interferometer [19] was located at $R=0.78$ m sampled at 2 kHz, while the signal changes lasted for no longer than a few tens of micro seconds. No measurable changes were observed.

Future work will study a wide range of discharges with different n_e etc, and make use of a more extensive set of pedestal diagnostics, in particular, edge Thomson Scattering, which have become available since the time of these measurements.

Acknowledgments

The authors would like to thank J. Heard for providing the O-mode radiometer data, M. Greenwald for useful discussion regarding ELMs, and B. LaBombard and J. Irby for comments on the particle loss estimation. The author (Y. In) is thankful to W. Suttrop for providing ASDEX-U information and to A. Kritz and P. Bonoli for helping him resuscitate TORAY code in VAX environment. Without the successful operation of the whole Alcator C-Mod group, no parts in this paper could have been available. This work has been supported by USDOE Cooperative Agreement DE-FC02-99ER54512.

References

- [1] Connor J W 1998 *Plasma Phys. Control. Fusion* **40** 191
- [2] Zohm H 1996 *Plasma Phys. Control. Fusion* **38** 105
- [3] Wilson H R, Connor J W, Field A R, Fielding S J, Miller R L, Lao L L, Ferron J R and Turnbull A D 1999 *Phys. Plasmas* **6** 1925

- [4] Kamada Y, Hatae T, Fukuda T and Takizuka T 1999 *Plasma Phys. Control. Fusion* **41** 1371
- [5] Breger P, Flewin C, Zastrow K D *et al* 1998 *Plasma Phys. Control. Fusion* **40** 347
- [6] Groebner R J and Osborne T H 1998 *Phys. Plasmas* **5** 1800
- [7] Suttrop W, Gruber O, Kurzan B, Murmann H D, Schweinzer J, Stober J, Treutterer W and ASDEX Upgrade Team 1999 Proceedings of the 26th EPS Conf. on Contr. Fusion and Plas. Phys. **23J** 1405
- [8] Hubbard A E, Boivin R L, Granetz R S *et al* 1998 *Phys. Plasmas* **5** 1744
- [9] Suttrop W, Buchl K, de Blank H J, Schweinzer J, Zohm H, ASDEX Upgrade team, NBI group and ICRH group 1996 *Plasma Phys. Control. Fusion* **38** 1407
- [10] In Y, Boivin R L, Granetz R, Greenwald M, Hubbard A, Hutchinson I, Irby J, Ramos J and Snipes J 1998 *Bull. Am. Phys. Soc.* **43** 1820
- [11] Hutchinson I H, Boivin R, Bombarda F *et al* 1994 *Phys. Plasmas* **1** 1511
- [12] Batchelor D B, Goldfinger R C and Weitzner H 1980 *IEEE Trans. on Plasma Science* **PS-8** 78
- [13] Dimock D *et al* 1997 *Rev. Sci. Instrum.* **68** 700
- [14] Hubbard A E *et al* 2001 *Pedestal profiles and fluctuations in C-Mod enhanced D-alpha H-modes*, to appear in *Phys. Plasmas*
- [15] In Y 2000 PhD thesis, MIT
- [16] Hsu T H 1993 PhD thesis, MIT; Hsu *et al* 1993 *Proc. of Eighth Joint Workshop on ECE and ECRH (Gut Ising, Germany, 1992)* vol 2 (IPP) p 409
- [17] Barnhart D 1995 *Optica*, Wolfram Research Inc.
- [18] Hutchinson I H 1987 *Principles of Plasma Diagnostics*, Cambridge University Press
- [19] Irby J H, Marmor E S, Sevillano E and Wolfe S M 1988 *Rev. Sci. Instrum.* **59** 1568